AVS Quantum Science

RESEARCH ARTICLE | NOVEMBER 17 2023

Quantum diamond microscope for dynamic imaging of magnetic fields

Jiashen Tang ; Zechuan Yin ; Connor A. Hart ; John W. Blanchard ; Jner Tzern Oon ; Smriti Bhalerao ; Jennifer M. Schloss ; Matthew J. Turner ; Ronald L. Walsworth

AVS Quantum Sci. 5, 044403 (2023)
https://doi.org/10.1116/5.0176317

Quantum diamond microscope for dynamic imaging of magnetic fields

Cite as: AVS Quantum Sci. 5, 044403 (2023); doi: 10.1116/5.0176317
Submitted: 12 September 2023 · Accepted: 30 October 2023 ·
Published Online: 17 November 2023

View Online Export Citation CrossMark

Jiashen Tang,[1,2] Zechuan Yin,[2,3] Connor A. Hart,[2,3] John W. Blanchard,[2,3] Jner Tzern Oon,[1,2] Smriti Bhalerao,[4] Jennifer M. Schloss,[5] Matthew J. Turner,[2,3] and Ronald L. Walsworth[1,2,3,a)]

AFFILIATIONS

[1]Department of Physics, University of Maryland, College Park, Maryland 20742, USA
[2]Quantum Technology Center, University of Maryland, College Park, Maryland 20742, USA
[3]Department of Electrical Engineering and Computer Science, University of Maryland, College Park, Maryland 20742, USA
[4]Fischell Department of Bioengineering, University of Maryland, College Park, Maryland 20742, USA
[5]Lincoln Laboratory, Massachusetts Institute of Technology, Lexington, Massachusetts 02421, USA

[a)]Author to whom correspondence should be addressed: walsworth@umd.edu

ABSTRACT

Wide-field imaging of magnetic signals using ensembles of nitrogen-vacancy (NV) centers in diamond has garnered increasing interest due to its combination of micron-scale resolution, millimeter-scale field of view, and compatibility with diverse samples from across the physical and life sciences. Recently, wide-field NV magnetic imaging based on the Ramsey protocol has achieved uniform and enhanced sensitivity compared to conventional measurements. Here, we integrate the Ramsey-based protocol with spin-bath driving to extend the NV spin dephasing time and improve magnetic sensitivity. We also employ a high-speed camera to enable dynamic wide-field magnetic imaging. We benchmark the utility of this quantum diamond microscope (QDM) by imaging magnetic fields produced from a fabricated wire phantom. Over a $270 \times 270\ \mu m^2$ field of view, a median per-pixel magnetic sensitivity of $4.1(1)\ \mathrm{nT}/\sqrt{\mathrm{Hz}}$ is realized with a spatial resolution $\lesssim 10\ \mu m$ and sub-millisecond temporal resolution. Importantly, the spatial magnetic noise floor can be reduced to the picotesla scale by time-averaging and signal modulation, which enables imaging of a magnetic-field pattern with a peak-to-peak amplitude difference of about 300 pT. Finally, we discuss potential new applications of this dynamic QDM in studying biomineralization and electrically active cells.

I. INTRODUCTION

The nitrogen-vacancy (NV) center in diamond is a solid-state spin defect that emits magnetic-field-dependent fluorescence under optical excitation. Precision magnetic sensing can be performed at ambient conditions using an ensemble of NVs or a single NV, with wide-ranging applications across the physical and life sciences.[1–3] In particular, the wide-field magnetic imaging modality known as the quantum diamond microscope (QDM) employs a dense, micron-scale-thick surface layer of NVs on a diamond chip, onto which a sample of interest is placed. The QDM has been applied for studying both static and dynamic magnetic signals from diverse samples, including ancient rocks and meteorites, 2D condensed matter systems, and electronic circuits.[1,4–6] The QDM is also useful for many life science applications, due to the biocompatibility of the diamond surface. Examples include characterization of iron mineralization in bacteria,[7] malarial hemozoin crystals,[8] and iron organelles in homing pigeons;[9] understanding the microscopic origin of MRI contrast;[10] and tracking the tumbling dynamics of DNA-tethered magnetic particles[11] among other applications.[12–14]

A majority of QDMs realized to date utilize a continuous-wave optically detected magnetic resonance (CW-ODMR) sensing protocol. However, competing effects of the optical and microwave (MW) fields employed during CW-ODMR measurements constrain the achievable sensitivity for a fixed number of NVs per imaging pixel.[2] This limitation results in averaging intervals of hours for nanotesla magnetic fields,[7,9,10] restricting the imaging of weaker magnetic sources, as well as sample throughput. The demand for sensitivity is especially critical when both spatial and time resolution are required for imaging dynamic magnetic fields, such as from action potential (AP) currents in electrically active cells. To date, dynamic NV-based measurements have detected magnetic fields from neuron,[15] cardiac,[16] and muscle[14] AP currents, but only by spatially integrating the ensemble NV fluorescence (over $> 100\ \mu m$ length scales) onto a single photodiode and signal averaging over multiple AP measurements. In particular, the

temporal resolution in demonstrated QDM dynamic biomagnetic imaging experiments[10,11] are inadequate compared to the sub-millisecond timescales required for resolving individual AP currents.

QDM per-pixel magnetic sensitivity and temporal resolution can be improved by implementing a pulsed sensing protocol with acquisition using a high-frame-rate camera.[17–19] Pulsed protocols using Ramsey magnetometry, in particular, separate intervals of NV optical preparation and readout, MW control, and sensing, affording optimization of each NV-interrogation stage for improved sensitivity compared to CW-ODMR. Recent advances in Ramsey-based magnetic imaging protocols have demonstrated robustness to errors from heterogeneous MW control fields, diamond strain, and temperature,[17] enabling spatially uniform and order-of-magnitude improved sensitivity compared to CW-ODMR-based measurements.[6]

In this work, we benchmark the utility of a Ramsey-based QDM using a high-speed, lock-in camera by imaging static and dynamic magnetic fields from a fabricated wire phantom [Fig. 1(a)]. The phantom's geometry is designed to generate nontrivial, micron-scale spatial patterns of magnetic fields. We additionally integrate spin-bath driving[20] to improve the magnetic sensitivity by extending the NV spin dephasing time, expanding the utility of this technique from previous confocal-volume demonstrations to wide-field imaging. After describing the experimental setup in Sec. II, we first characterize the performance of the magnetic imaging system, including analysis of sensitivity in Sec. III A and spatial magnetic noise floor in Sec. III B. Next, we present static magnetic-field imaging experiments with micron-scale spatial resolution in Sec. III C. Importantly, we demonstrate the capability to resolve a picotesla-scale magnetic-field pattern by time-averaging and signal modulation and show the usefulness of a denoising technique[21] in improving the image signal-to-noise ratio (SNR). In Sec. III D, we image dynamic magnetic fields by applying to the phantom a broadband, synthetic human cardiac signal. We show that a time series of QDM magnetic images can capture temporal variations with sub-millisecond time resolution. Given these demonstrations, we discuss potential applications in imaging static and dynamic biomagnetic signals in Sec. IV, including magnetic characterization of iron-loaded compartments in engineered eukaryotic cells,[22] high-throughput screening of biogenic magnetite across candidate tissues for vertebrate magnetoreceptors,[9,23–25] and monitoring of currents in cardiomyocytes. Finally, we provide an outlook toward imaging weaker and more transient biomagnetic fields such as signals produced by neuronal currents.

II. EXPERIMENTAL METHODS

The NV center is a C_{3v}-symmetric defect center formed by substitution of a nitrogen atom adjacent to a vacancy in the diamond lattice. Its electronic spin $S = 1$ ground state [Fig. 1(b)] has a zero-field splitting $D = 2\pi \times 2.87$ GHz at room temperature, separating the $|m_s = 0\rangle$ and $|m_s = \pm 1\rangle$ sublevels. Application of a bias magnetic field further splits the degenerate $|m_s = +1\rangle$ and $|m_s = -1\rangle$ states through the Zeeman effect. For the present QDM experiments, a nominal 4.3 mT bias magnetic field is aligned to one of the four NV ensemble axes in diamond for sensing the projection of signal magnetic fields along that particular sensing NV axis (defined as the z axis). Under this condition, transverse crystal stress and electric fields can be neglected in the ground-state sensing NV Hamiltonian,[17,26–28] resulting in the approximate form

$$\hat{H}/\hbar \approx [D + M_z]\hat{S}_z^2 + \gamma B_z \hat{S}_z, \tag{1}$$

where $\hat{S}_z$ is the dimensionless spin-1 operator, $\gamma = 2\pi \times 28.024$ GHz/T (Ref. 29) is the NV electron gyromagnetic ratio, and B_z and M_z are longitudinal components of the bias magnetic field and crystal stress, respectively. (More generally, vector magnetic sensing is possible by measuring the components of the signal field along all NV axes.[2])

The sequence employed for magnetic imaging is shown in Fig. 1(c), and the experimental apparatus is shown schematically in Fig. 1(d). The diamond employed in these demonstration experiments has a 10 μm NV

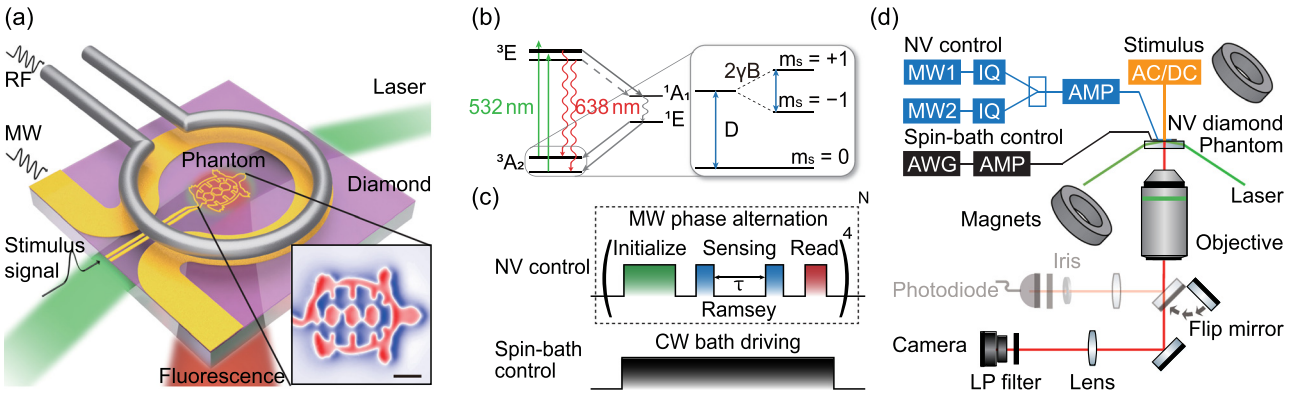

Fig. 1. (a) Imaging phantom magnetic fields using a quantum diamond microscope (QDM). 532-nm excitation laser light excites NV centers at the diamond chip surface. A planar, gold omega-loop delivers microwaves (MWs) to the diamond chip for NV spin-state control. Optical components collect NV fluorescence onto either a photodiode or a high-speed camera (not shown). A bias magnetic field (not shown) is applied along one NV axis. An RF signal delivered by a nearby coil drives paramagnetic bath spins in the diamond to increase the ensemble NV spin dephasing time (T_2^*). A driven current in the phantom produces a magnetic-field pattern to be imaged with the QDM. An example image of simulated phantom magnetic signals, projected along the direction of a sensing NV axis with 5 μm standoff from the source to the NV surface, is shown in the inset. Scale bar: 50 μm. (b) NV energy-level diagram. The enlarged view shows the electronic spin triplet ground state with zero-field splitting D and bias magnetic field B aligned to the sensing NV axis. (c) Pulse sequence for magnetic imaging based on integration of Ramsey magnetometry (top) and spin-bath driving (bottom). To mitigate NV control error and laser intensity noise, a dual-tone MW is employed, and its phase is alternated (see main text). (d) Experimental apparatus. A flip mirror can route the NV fluorescence to a photodiode for rapid measurements of ensemble NV spin properties and experimental optimization.

ensemble layer ([NV] = 2.4 ppm, ^{15}N enriched) on a $2 \times 2 \times 0.5$ mm^3 substrate (> 99.995% ^{12}C). During the Ramsey sequence, a pulse of 532 nm laser irradiation first initializes the NV electronic spin state to $|m_s = 0\rangle$ via optical pumping. Then, a dual-tone MW pulse prepares the NV spin state as a superposition between $|m_s = +1\rangle$ and $|m_s = -1\rangle$ for magnetic sensing. In the subsequent Ramsey free evolution interval τ, the presence of an additional signal magnetic field B_{sig} along the sensing NV axis causes accumulation of a relative phase $\phi_B = 2\gamma B_{sig}\tau$ between $|m_s = +1\rangle$ and $|m_s = -1\rangle$ in the rotating frame.[30] The optimal choice[2] of τ is limited by the NV spin dephasing time T_2^*. To extend T_2^* while retaining sensitivity to static and broadband magnetic signals, RF control fields resonant with the paramagnetic spin-bath transitions in the diamond are applied during the free evolution interval. This spin-bath-driving technique decouples unwanted dipolar interactions between NV sensor spins and paramagnetic bath spins (Sec. III in the supplementary material). At the end of the Ramsey free evolution interval, a second dual-tone MW pulse maps the accumulated phase information ϕ_B into a population difference between $|m_s = 0\rangle$ and $|m_s = \pm 1\rangle$. This population difference, proportional to the magnetic signal B_{sig}, is subsequently read out using the spin-state-dependent NV fluorescence via a lock-in camera (Heliotis heliCam^{TM} C3) that is capable of external frame rate of up to 3.8 kHz. The camera has a tunable internal exposure frequency of up to 1 MHz, which is synchronized with MW-phase-alternated Ramsey measurements. This particular variation of the Ramsey sequence is designed to mitigate laser intensity noise and NV spin-control errors in the accumulated signal contained in each external frame (Sec. II in the supplementary material). A 270×270 μm^2 region of the NV layer is selected as the field of view, where each pixel corresponds to a lateral area of about 1.9×1.9 μm^2. In the following experiments, up to 3×3 pixel binning is applied such that the magnetic spatial resolution is expected to be limited by the 10-μm-thick NV layer. Additional details regarding the experimental setup are provided in Sec. I of the supplementary material.

III. RESULTS

A. NV spin dephasing time and magnetic sensitivity

We first characterize the performance of the Ramsey-based QDM with and without spin-bath driving. The NV spin dephasing time T_2^* and magnetic-field sensitivity η are studied on a pixel-by-pixel basis over the field of view. For these measurements, a dual-tone MW implementation of the Ramsey sequence leverages a strain- and temperature-insensitive coherence (Sec. II in the supplementary material) such that the NV ensemble T_2^* is limited by dipolar interactions with bath spins. Under this condition, spin-bath driving improves the NV spin dephasing time and magnetic sensitivity as shown in Fig. 2(a). The median per-pixel T_2^* is extended by about 1.8× to 2.2(1) μs, approaching the estimated NV–NV interaction limit of 2.5 μs for this sample (Sec. IV in the supplementary material). The median per-pixel η is enhanced by about 2.4× to 4.1(1) nT $/\sqrt{\text{Hz}}$ in the absence of pixel binning and is comparable to the combined quantization and photon-shot-noise-limited sensitivity estimate of 3.2 nT$/\sqrt{\text{Hz}}$ (in roughly equal contribution, Sec. IV in the supplementary material). For photon shot-noise-limited Ramsey magnetometry, the magnetic sensitivity can be written as[2] [also see Eq. (S5) in the supplementary material] $\eta_{shot} \propto \sqrt{t_D + \tau}/\tau C e^{(-\tau/T_2^*)^p}$, where C is the NV spin-state readout contrast, τ is the Ramsey free evolution interval, p is a parameter used to describe the Ramsey envelope decay shape, and τ_D is the overhead time for NV initialization and readout. The present QDM

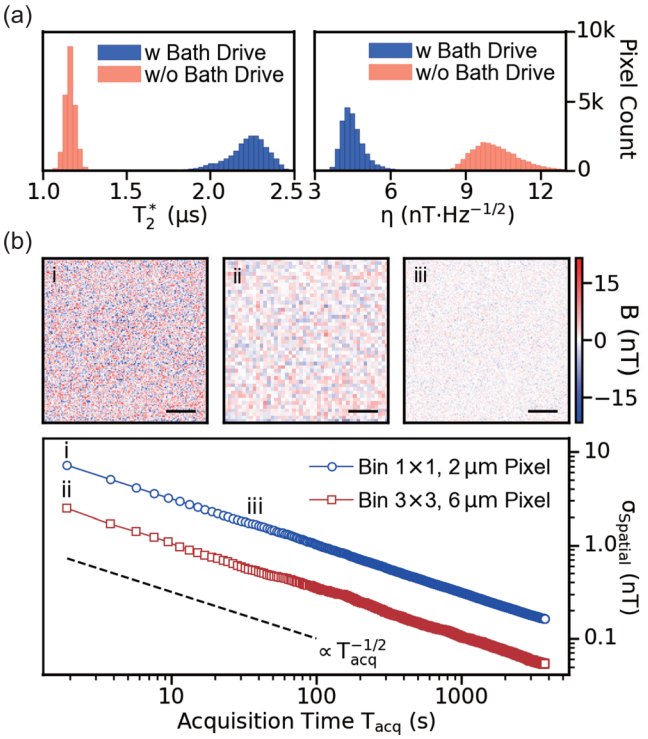

FIG. 2. Measured magnetic sensing performance of the Ramsey-based QDM. (a) Median per-pixel T_2^* is 2.2(1) and 1.2(1) μs with and without spin-bath driving. Median per-pixel η is 4.1(1) and 9.4(1) nT $/\sqrt{\text{Hz}}$ with and without spin-bath driving. (b) Spatial magnetic noise floor. Measurement data are obtained using the differential measurement protocol (see main text). Top: Images of magnetic noise with different acquisition times and pixel binning (see the bottom plot). Here, the acquisition time accounts for the duration of time spent acquiring measurements, but excludes the implementation-dependent time required to transfer and store data from the camera to a host computer. The magnetic noise is distributed randomly without significant spatial correlation. Field of view: 270×270 μm^2. Scale bar: 50 μm. Bottom: spatial magnetic noise floor $\sigma_{spatial}$ as a function of acquisition time T_{acq} for no pixel binning and 3×3 pixel binning. $\sigma_{spatial}$ is computed as the standard deviation of magnetic-field measurements using the entire image after any pixel binning. A dashed black line depicts power law scaling behavior $\propto T_{acq}^{-1/2}$ as a guide to the eye.

operates in a regime where the sensitivity nominally improves linearly with increased dephasing time,[2,20] as $\tau_D = 7.04$ μs is longer than the sensing interval $\tau \approx T_2^*$, yielding $\eta_{shot} \propto \sqrt{t_D}/\tau C$. The additional superlinearity of the measured η improvement is attributed to an observed increase in spin-state readout contrast C of about 1.2× when using spin-bath driving and the discrete choices of τ due to Ramsey fringe beating introduced by the hyperfine splitting of the NV spin resonances.[17]

The measured per-pixel magnetic sensitivity describes the expected magnetic noise after 1 s of signal acquisition. Here, the signal acquisition time T_{acq} accounts for the duration of time allocated to acquiring measurements, but excludes the implementation-dependent duration required to transfer and store the data from the 500-frame camera buffer to a host computer (Sec. I in the supplementary material). This technical overhead is included below when reporting a "wall-clock" time T_{wall}. The frame rates, wall-clock times, and Allan

deviations associated with magnetic sensitivity results in Fig. 2(a) are included in Sec. IV of the supplementary material.

B. Spatial magnetic noise floor

In magnetic imaging, the ability to resolve a signal of interest depends upon the per-pixel magnetic sensitivity and spatial magnetic noise floor.[4] Similar to Ref. 4, we quantify the spatial magnetic noise floor σ_{spatial} after a certain acquisition time by calculating the standard deviation of magnetic-field measurements across the time-averaged image without any external signal sources present. Uncorrelated spatial noise can be time-averaged. However, correlated spatial noise across an image, particularly when similar to the length scale of the signal of interest, inhibits the utility of temporal averaging and limits the minimum resolvable magnetic field. Specifically, vibration and temperature changes can induce spatial and temporal variations in the bias magnetic field and optical illumination intensity, thereby introducing correlated noise into QDM magnetic images.

For QDM magnetic images of an external signal source (such as the phantom used in the present demonstration experiments), we mitigate the impact of spatially correlated noise varying slowly on the timescale between acquisitions of frame sets (i.e., the time required to transfer the collected 500 frames to the host computer) by employing a differential measurement protocol. Currents in the phantom are modulated after one acquisition of the 500-frame set by either on–off gating or reversing the polarity (Sec. V in the supplementary material). This protocol enables long-term averaging and is applicable to studies of signals that can be externally controlled, e.g., from electronic circuits and electrically active biological cells. When studying signal sources that cannot be varied straightforwardly, alternative protocols such as modulating the polarity of bias magnetic field, more advanced MW pulse sequence schemes, or post-processing filtering can be employed to mitigate the spatially correlated noise.[15,31,32]

As shown in Fig. 2(b), the spatial distribution of noise in QDM images, at different acquisition times T_{acq} and with no current flowing in the phantom, have insignificant correlation when using the differential measurement protocol. The spatial magnetic noise floor, $\sigma_{spatial}$, can be averaged down as reflected in the observed $\sigma_{spatial} \propto T_{acq}^{-1/2}$ scaling persistent up to about $T_{acq} = 4000$ s ($T_{wall} \approx 8$ h). An inverse proportionality $\sigma_{spatial} \propto 1/n_{bin}$ is observed as $n_{bin} \times n_{bin}$ pixels are averaged, allowing spatial resolution to be traded for improved spatial magnetic noise floor and reduced acquisition time. Additional spatial magnetic noise floor measurements, for different pixel binning and without employing the differential measurement protocol, are included in Secs. V and VI of the supplementary material, respectively.

C. Static magnetic-field imaging

We characterize the capability of the Ramsey-based QDM to image static magnetic fields by applying steady currents to the fabricated wire phantom. The polarity of applied signals is reversed between acquisitions of frame sets to allow differential measurements (Sec. V in the supplementary material). As shown in Fig. 3(a), an imaged magnetic-field pattern with a peak-to-peak amplitude difference of about 14 nT is obtained by supplying a fixed voltage of 25 mV (436 nA current) to the phantom and averaging for about $T_{acq} = 200$ s ($T_{wall} \approx 21$ min). We simulate the expected phantom magnetic-field pattern by using finite element software (COMSOL Multiphysics®)[33]

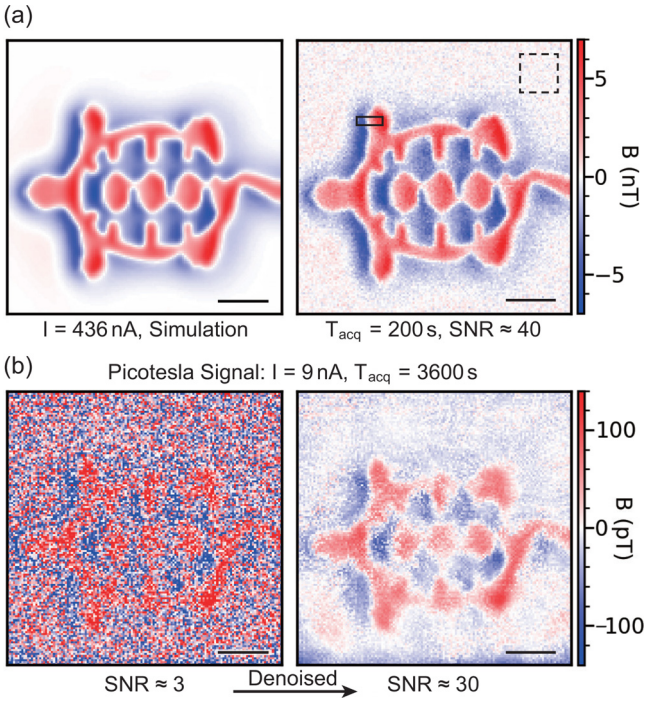

FIG. 3. (a) Simulated (left) and measured (right) phantom static magnetic-field patterns using the Ramsey-based QDM and a differential measurement protocol. The measurement is conducted with a 25 mV voltage (436 nA current) applied to the phantom and time-averaged for about 200 s. To compute SNR, the peak-to-peak amplitude difference of the magnetic-field pattern (solid box) is divided by the spatial magnetic noise obtained from a source-free region (dashed box). The simulated phantom magnetic-field pattern is obtained using the applied current and geometry of the phantom. To mimic the parameters of the imaging system, the simulated magnetic fields are further averaged over a depth of 10 μm (the NV-layer thickness) and binned with a pixel area of 1.9×1.9 μm^2. NV-phantom standoff distance is the only free parameter and is tuned to a value of 5 μm to best match the measured magnetic-field pattern. (b) Demonstration of a picotesla-scale QDM magnetic image. Left: after about $T_{acq} = 3600$ s ($T_{wall} \approx 7$ h) time-averaging, a magnetic-field pattern with a peak-to-peak amplitude difference of about 300 pT is resolved with SNR ≈ 3. Right: applying a non-local mean denoising technique enhances image SNR by about 10×. All images are not binned, and scale bars are 50 μm for (a) and (b).

to calculate the current density distributions and the accompanying magnetic signals, given the phantom geometry and experimental input current I. The standoff distance d_{so} between the phantom and NV surface is the only free parameter in the simulation and is chosen to best match the measured magnetic-field pattern,[34] yielding $d_{so} \approx 5$ μm. Additional simulated phantom magnetic-field patterns projected along different NV crystal axes are shown in the supplementary material, Sec. IX.

We also demonstrate QDM magnetic imaging of a picotesla-scale signal by applying a 500 μV voltage (9 nA current) to the phantom. After averaging for about $T_{acq} = 3600$ s ($T_{wall} \approx 7$ h), a phantom magnetic-field pattern with a peak-to-peak amplitude difference of about 300 pT is resolved with SNR ≈ 3 as shown in Fig. 3(b), left panel. In addition, as the magnetic noise has insignificant pixel-to-pixel correlation [Fig. 2(b)], we can apply image denoising techniques to enhance SNR. A non-local mean denoising method[21,35,36] (Sec. VII in the supplementary material) implemented in open-source

software[37] enables an order-of-magnitude improvement of SNR, as seen in Fig. 3(b), right panel.

D. Dynamic magnetic-field imaging

Access to individual frames from the QDM's lock-in camera permits imaging of dynamic magnetic signals. As an example, we apply a 1 s-long broadband voltage trace, mimicking a human cardiac signal, to the phantom and image the associated temporal variations of the magnetic-field patterns. The camera external frame rate F_s is set to about 0.5 kHz to maximize time resolution while balancing the 500-frame camera buffer limitation on a continuous acquisition (Sec. I in the supplementary material). The signals applied to the phantom are gated between on and off across successive acquisitions of frame sets (Sec. V in the supplementary material). The experiment is repeated 400 times.

Figure 4 displays the imaged dynamic magnetic fields with 3×3 pixel binning (spatial resolution $\lesssim 10\,\mu$m). The applied voltage trace is shown in Fig. 4(a) and overlaid with the measured peak magnetic-field amplitude. To demonstrate the capability of high-fidelity waveform-reconstruction, the entire voltage trace is multiplied with a voltage-to-magnetic-field scaling factor obtained from the applied voltage and measured peak magnetic-field amplitude data in the static imaging experiment [Fig. 3(a)]. The good agreement shown in Fig. 4(a) motivates possible applications such as comparison with patch clamp electrophysiology recording. A series of magnetic images at time points corresponding to the pseudo-cardiac signal local extrema are shown in Fig. 4(b). The phantom magnetic-field pattern becomes indistinguishable from the background at (vi), which is used to obtain the spatial magnetic noise floor $\sigma_{spatial} \approx 3$ nT.

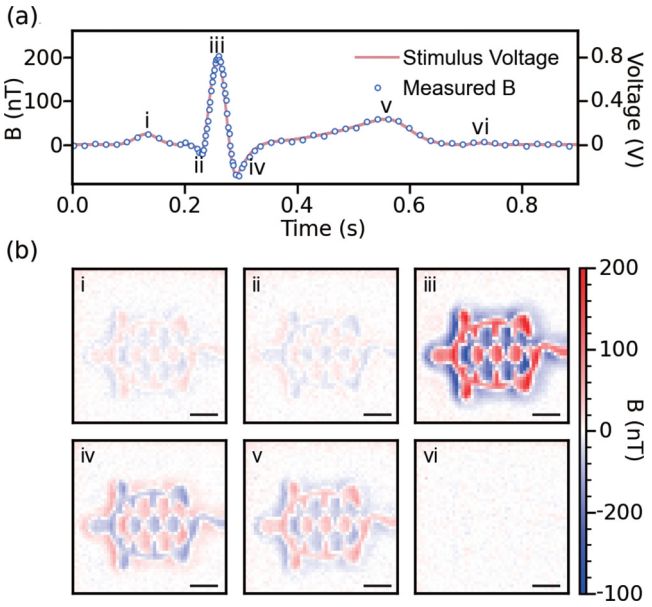

Fig. 4. Time-resolved imaging of dynamic magnetic fields using the Ramsey-based QDM and a differential measurement protocol. A voltage trace mimicking a synthetic, broadband human cardiac signal is applied to the phantom. Sets of QDM magnetic images are collected with temporal resolution of about 2 ms and binned with 3×3 pixels. The experiments are repeated 400 times to allow signal averaging. (a) Temporal variation of the peak magnetic field from the signal-averaged images is overlaid with the applied stimulus. A voltage-to-magnetic-field scaling factor of 274.26 nT/V is applied to the entire voltage trace (see main text). A subset of peak magnetic-field amplitudes from the acquired images are displayed, indicating good agreement between the applied voltages and magnetic measurements. (b) Selected magnetic-field images at time points labeled in (a). Each image has been signal averaged. The spatial magnetic noise at time (vi) is about 3 nT.

Magnetic imaging with sub-millisecond time resolution is also feasible with the present QDM, as the external frame rate F_s can be increased to 3.8 kHz. As an example, single-frequency oscillating voltages (<Nyquist frequency, $F_s/2$) are applied to the phantom, with measured results shown in Sec. VIII of the supplementary material.

IV. DISCUSSION

We demonstrate a quantum diamond microscope (QDM) for sensitive, high-speed wide-field imaging of static and broadband magnetic signals, based on Ramsey magnetometry and spin-bath-driving techniques. The dual-tone MW implementation of the Ramsey sequence mitigates sensitivity degradation due to heterogeneous MW control fields and diamond strain, while spin-bath driving further extends the NV spin dephasing time and improves magnetic sensitivity by decoupling NV interactions with bath spins. Over a $270 \times 270\,\mu$m^2 field of view, a median per-pixel magnetic sensitivity of 4.1(1) nT $/\sqrt{\text{Hz}}$ is realized; and the spatial magnetic noise floor can be averaged down to the picotesla scale using a differential measurement protocol. In addition, the QDM's lock-in camera permits time-resolved magnetic imaging with sub-millisecond temporal resolution.

The Ramsey-based QDM presented in this work is a key step toward applications in the physical and life sciences. For example, magnetic-particle-based studies using previous QDMs have probed nanotesla signal amplitudes.[10–12] The sensitivity achieved with the present QDM should allow studies of picotesla-scale signal amplitudes. As an example of detecting weak biomagnetic signals, iron-loaded bacterial encapsulin compartments expressed in genetically engineered mammalian cells are of interest.[22] Magnetization in such 30 nm-diameter shell structures has been demonstrated to produce beneficial T_2 contrast in MRI. Cellular engineering to enhance iron loading, and, in particular, to screen for superparamagnetism, can facilitate optimization of such MRI contrast agents. Assuming volumetric magnetization similar to commercial superparamagnetic iron-oxide nanoparticles,[10] an engineered 30 nm-diameter compartment is expected to produce a magnetic field ~600 pT at a 10 μm standoff, which can be resolved by the Ramsey-based QDM within a reasonable averaging time (~100 s of signal acquisition).

The Ramsey-based QDM could also function as a high-throughput biomagnetism tool, such as searches for biogenic magnetite particles related to vertebrate magnetoreception[38] or population-based measurements. The localization of cells containing magnetite has been challenging, as organism-scale volumes of candidate tissues need to be screened. Successful identification of magnetite in salmon[23,39] using magnetic force microscopy suggests an order-of-magnitude estimate for the dipole moment of 10^{-16} A m^2. Assuming magnetite in other model animals has similar dipole moments, the magnetic field magnitude immediately outside a 10 μm cell is expected to be tens of nanotesla, which can be imaged by the present QDM with SNR $\approx$ 10 in a few minutes of signal averaging [see Fig. 3(a)]. We estimate a tissue area magnetite screening rate of a few mm^2 per hour using the present QDM, assuming a 10 μm-thick tissue. In addition, the QDM's ability to measure spatial distributions of vector magnetic fields enables quantitative estimations of dipole moments.[7,10] We thus

expect the QDM may become a promising tool for the rapid screening of vertebrate magnetoreceptor cells.

Beyond imaging of static magnetic fields, the Ramsey-based QDM's capability to measure temporal dynamics can benefit studies of electrically active cells. For example, spatially resolved measurements of electrical currents in cardiac tissue—via imaging of induced dynamic magnetic fields—could inform biophysics modeling at the cellular level[40–42] or aid in pharmaceutical studies.[43] Previous measurements of the heart have recorded nanotesla-scale magnetic fields at $>100\,\mu$m standoff distances.[16,44] As the NV sensing layer can be brought to few micrometer standoff distances from live bio-samples[15] and externally controlled currents ($\gtrsim 1\,\mu$A) can be applied to cardiac tissue,[45] we expect that the Ramsey-based QDM may find applications in mapping the microscopic electrical properties of such tissue.[46,47]

The sub-millisecond time resolution of the present QDM (Sec. VIII in the supplementary material) is sufficient for mapping the dynamic magnetic fields produced by neuronal action potential (AP) currents.[48] However, resolving the expected $\lesssim 1$ nT AP magnetic signal[49] with a $\sim$0.5 ms temporal resolution requires $\gtrsim 4$ k averages ($\gtrsim 2$ day of wall-clock time) to reduce the spatial magnetic noise floor $\sigma_{spatial}$ to $\lesssim 0.8$ nT using 5×5 pixel binning ($\sim 10 \times 10 \times 10\ \mu\text{m}^3$ sensing volume) with the present sensitivity and technical overhead time. While repeated AP excitation of cultured neurons *in vitro* is feasible (continuous stimulation at 4 Hz over days has been reported[50]), the long experimental time poses a significant challenge. For the QDM to become an attractive tool for this application, at least an order-of-magnitude improvement in volume-normalized (i.e., per-pixel) sensitivity is likely required. In the present system, increasing the optical illumination intensity for improved NV fluorescence signal results in degraded contrast due to NV charge-state conversion.[51] The optimal laser illumination intensity found in the present work $\sim 0.014\ \text{mW}/\mu\text{m}^2$ is far from the NV saturation intensity[52] ($1 - 3\ \text{mW}/\mu\text{m}^2$), highlighting the importance of further diamond engineering to mitigate charge-state issues. The ensemble NV spin dephasing time after spin-bath driving $T_2^* = 2.2(1)\ \mu$s is limited by NV–NV dipolar interactions. Homonuclear-decoupling techniques[53] that mitigate NV–NV interactions while maintaining sensitivity to static and broadband magnetic fields are promising for further NV T_2^* extension. Beyond the direct sensitivity improvements due to prolonged NV spin dephasing time, improving the sensing duty cycle in the pulse sequence (i.e., increasing the fraction of time spent in the Ramsey free evolution interval) may warrant the use of alternative readout schemes;[2] and may require further advances in camera and other hardware capabilities. In particular, reducing the overhead time associated with data transfer from the camera buffer to the host computer will be a key challenge for future QDM optimization.

While we focus in this work on imaging the projected component of magnetic signals along a single sensing NV orientation, vector magnetic-field imaging can be also realized by sequentially interrogating the four different NV axes.[1] In addition, pulsed protocols for NV AC magnetometry[54] may enable wide-field imaging of thermally polarized NMR signals with micron-scale resolution. Quantum logic enhanced (QLE) techniques for NV ensembles have recently demonstrated $>10\times$ SNR enhancement for AC signals.[55] QLE sensing may also be incorporated in future QDM realizations.

SUPPLEMENTARY MATERIAL

See the supplementary material for additional details of experimental methods.

ACKNOWLEDGMENTS

We thank David R. Glenn and Pauli Kehayias for helpful comments and discussion in preparing the manuscript. We acknowledge the support of the Maryland NanoCenter and its FabLab. This work was supported by, or in part by, the U.S. Army Research Laboratory under Grant No. W911NF1510548 and Contract No. W911NF1920181; the U.S. Army Research Office under Grant No. W911NF2120110; the DARPA DRINQS program under Grant No. D18AC00033; the National Science Foundation (NSF) Center for Integration of Modern Optoelectronic Materials on Demand (IMOD) via Grant No. DMR-2019444; the U.S. Air Force Office of Scientific Research under Grant No. FA9550-22-1-0312; the Gordon & Betty Moore Foundation under Grant No. 7797.01; and the University of Maryland Quantum Technology Center.

AUTHOR DECLARATIONS

Conflict of Interest

Yes, Ronald L. Walsworth is a founder of and advisor to companies that are developing and commercializing NV-diamond technology. These relationships are disclosed to and managed by the University of Maryland Conflict of Interest Office.

Author Contributions

Jiashen Tang and Zechuan Yin contributed equally to this work.

Jiashen Tang: Data curation (lead); Formal analysis (equal); Investigation (equal); Software (equal); Writing – original draft (lead); Writing – review & editing (equal). **Zechuan Yin:** Formal analysis (equal); Investigation (equal); Software (equal); Validation (equal); Visualization (lead); Writing – review & editing (equal). **Connor A. Hart:** Conceptualization (equal); Resources (equal); Validation (equal); Writing – review & editing (equal). **John W. Blanchard:** Resources (equal); Validation (equal); Writing – review & editing (equal). **Jner Tzern Oon:** Software (equal); Validation (equal); Writing – review & editing (equal). **Smriti Bhalerao:** Validation (equal); Writing – review & editing (equal). **Jennifer M. Schloss:** Conceptualization (equal); Writing – review & editing (equal). **Matthew J. Turner:** Conceptualization (equal); Writing – review & editing (equal). **Ronald L. Walsworth:** Funding acquisition (lead); Resources (equal); Supervision (lead); Writing – review & editing (equal).

DATA AVAILABILITY

The data that support the findings of this study are available from the corresponding author upon reasonable request.

REFERENCES

[1]E. V. Levine, M. J. Turner, P. Kehayias, C. A. Hart, N. Langellier, R. Trubko, D. R. Glenn, R. R. Fu, and R. L. Walsworth, Nanophotonics **8**, 1945 (2019).
[2]J. F. Barry, J. M. Schloss, E. Bauch, M. J. Turner, C. A. Hart, L. M. Pham, and R. L. Walsworth, Rev. Mod. Phys. **92**, 015004 (2020).

[3]N. Aslam, H. Zhou, E. K. Urbach, M. J. Turner, R. L. Walsworth, M. D. Lukin, and H. Park, Nat. Rev. Phys. **5**, 157 (2023).
[4]D. R. Glenn, R. R. Fu, P. Kehayias, D. Le Sage, E. A. Lima, B. P. Weiss, and R. L. Walsworth, Geochem. Geophys. Geosyst. **18**, 3254 (2017).
[5]M. J. Ku, T. X. Zhou, Q. Li, Y. J. Shin, J. K. Shi, C. Burch, L. E. Anderson, A. T. Pierce, Y. Xie *et al.*, Nature **583**, 537 (2020).
[6]M. J. Turner, N. Langellier, R. Bainbridge, D. Walters, S. Meesala, T. M. Babinec, P. Kehayias, A. Yacoby, E. Hu *et al.*, Phys. Rev. Appl **14**, 014097 (2020).
[7]D. Le Sage, K. Arai, D. R. Glenn, S. J. DeVience, L. M. Pham, L. Rahn-Lee, M. D. Lukin, A. Yacoby, A. Komeili *et al.*, Nature **496**, 486 (2013).
[8]I. Fescenko, A. Laraoui, J. Smits, N. Mosavian, P. Kehayias, J. Seto, L. Bougas, A. Jarmola, and V. M. Acosta, Phys. Rev. Appl. **11**, 034029 (2019).
[9]R. W. de Gille, J. M. McCoey, L. T. Hall, J.-P. Tetienne, E. P. Malkemper, D. A. Keays, L. C. Hollenberg, and D. A. Simpson, Proc. Natl. Acad. Sci. U. S. A. **118**, e2112749118 (2021).
[10]H. C. Davis, P. Ramesh, A. Bhatnagar, A. Lee-Gosselin, J. F. Barry, D. R. Glenn, R. L. Walsworth, and M. G. Shapiro, Nat. Commun. **9**, 131 (2018).
[11]Z. Kazi, I. M. Shelby, H. Watanabe, K. M. Itoh, V. Shutthanandan, P. A. Wiggins, and K.-M. C. Fu, Phys. Rev. Appl. **15**, 054032 (2021).
[12]D. R. Glenn, K. Lee, H. Park, R. Weissleder, A. Yacoby, M. D. Lukin, H. Lee, R. L. Walsworth, and C. B. Connolly, Nat. Methods **12**, 736 (2015).
[13]J. M. McCoey, M. Matsuoka, R. W. de Gille, L. T. Hall, J. A. Shaw, J.-P. Tetienne, D. Kisailus, L. C. Hollenberg, and D. A. Simpson, Small Methods **4**, 1900754 (2020).
[14]L. Troise, N. W. Hansen, C. Olsson, J. L. Webb, L. Tomasevic, J. Achard, O. Brinza, R. Staacke, M. Kieschnick *et al.*, AVS Quantum Sci. **4**, 044402 (2022).
[15]J. F. Barry, M. J. Turner, J. M. Schloss, D. R. Glenn, Y. Song, M. D. Lukin, H. Park, and R. L. Walsworth, Proc. Natl. Acad. Sci. U. S. A. **113**, 14133 (2016).
[16]K. Arai, A. Kuwahata, D. Nishitani, I. Fujisaki, R. Matsuki, Y. Nishio, Z. Xin, X. Cao, Y. Hatano *et al.*, Commun. Phys. **5**, 200 (2022).
[17]C. A. Hart, J. M. Schloss, M. J. Turner, P. J. Scheidegger, E. Bauch, and R. L. Walsworth, Phys. Rev. Appl. **15**, 044020 (2021).
[18]M. J. Turner, "Quantum diamond microscopes for biological systems and integrated circuits," Ph.D. thesis (Harvard University, 2020).
[19]J. M. Schloss, "Optimizing nitrogen-vacancy diamond magnetic sensors and imagers for broadband sensitivity," Ph.D. thesis (Massachusetts Institute of Technology, 2019).
[20]E. Bauch, C. A. Hart, J. M. Schloss, M. J. Turner, J. F. Barry, P. Kehayias, S. Singh, and R. L. Walsworth, Phys. Rev. X **8**, 031025 (2018).
[21]A. Buades, B. Coll, and J.-M. Morel, Image Process. Line **1**, 208 (2011).
[22]F. Sigmund, C. Massner, P. Erdmann, A. Stelzl, H. Rolbieski, M. Desai, S. Bricault, T. P. Wörner, J. Snijder *et al.*, Nat. Commun. **9**, 1990 (2018).
[23]C. E. Diebel, R. Proksch, C. R. Green, P. Neilson, and M. M. Walker, Nature **406**, 299 (2000).
[24]S. H. Eder, H. Cadiou, A. Muhamad, P. A. McNaughton, J. L. Kirschvink, and M. Winklhofer, Proc. Natl. Acad. Sci. U. S. A. **109**, 12022 (2012).
[25]N. B. Edelman, T. Fritz, S. Nimpf, P. Pichler, M. Lauwers, R. W. Hickman, A. Papadaki-Anastasopoulou, L. Ushakova, T. Heuser *et al.*, Proc. Natl. Acad. Sci. U. S. A. **112**, 262 (2015).
[26]M. W. Doherty, N. B. Manson, P. Delaney, F. Jelezko, J. Wrachtrup, and L. C. Hollenberg, Phys. Rep. **528**, 1 (2013).
[27]P. Kehayias, M. J. Turner, R. Trubko, J. M. Schloss, C. A. Hart, M. Wesson, D. R. Glenn, and R. L. Walsworth, Phys. Rev. B **100**, 174103 (2019).
[28]P. Udvarhelyi, V. O. Shkolnikov, A. Gali, G. Burkard, and A. Pályi, Phys. Rev. B **98**, 075201 (2018).
[29]V. M. Acosta, E. Bauch, M. P. Ledbetter, A. Waxman, L.-S. Bouchard, and D. Budker, Phys. Rev. Lett. **104**, 070801 (2010).
[30]H. Mamin, M. Sherwood, M. Kim, C. Rettner, K. Ohno, D. Awschalom, and D. Rugar, Phys. Rev. Lett. **113**, 030803 (2014).
[31]R. R. Fu, B. A. Maher, J. Nie, P. Gao, T. Berndt, E. Folsom, and T. Cavanaugh, Geochem. Geophys. Geosyst. **24**, e2022GC010812 (2023).
[32]M. C. Marshall, R. Ebadi, C. Hart, M. J. Turner, M. J. Ku, D. F. Phillips, and R. L. Walsworth, Phys. Rev. Appl. **17**, 024041 (2022).
[33]COMSOL Multiphysics® v. 6.0, https://www.comsol.com/comsol-multiphysics (2021).
[34]P. Kehayias, E. Levine, L. Basso, J. Henshaw, M. S. Ziabari, M. Titze, R. Haltli, J. Okoro, D. Tibbetts *et al.*, Phys. Rev. Appl **17**, 014021 (2022).
[35]A. Buades, B. Coll, and J.-M. Morel, "A non-local algorithm for image denoising," in *IEEE Computer Society Conference on Computer Vision and Pattern Recognition (CVPR)* (IEEE, 2005), Vol. 2, pp. 60–65.
[36]A. Buades, B. Coll, and J.-M. Morel, Multiscale Model. Simul. **4**, 490 (2005).
[37]G. Bradski, Dr. Dobb's J. Software Tools **120**, 122 (2000).
[38]M. Winklhofer and J. L. Kirschvink, J. R. Soc. Interface **7**, S273 (2010).
[39]M. M. Walker, C. E. Diebel, C. V. Haugh, P. M. Pankhurst, J. C. Montgomery, and C. R. Green, Nature **390**, 371 (1997).
[40]K. H. Jaeger and A. Tveito, Front. Physiol. **12**, 2439 (2022).
[41]S. Rohr, Cardiovasc. Res. **62**, 309 (2004).
[42]S. Dhein and A. Salameh, Cells **10**, 2422 (2021).
[43]S. Barral and M. A. Kurian, Front. Mol. Neurosci. **9**, 78 (2016).
[44]J. R. Holzer, L. E. Fong, V. Y. Sidorov, J. P. Wikswo, and F. Baudenbacher, Biophys. J. **87**, 4326 (2004).
[45]S. Rossi, A. Buccarello, P. R. Ershler, R. L. Lux, S. Callegari, D. Corradi, L. Carnevali, A. Sgoifo, M. Miragoli *et al.*, Am. J. Physiol.: Heart Circ. Physiol. **312**, H584 (2017).
[46]N. G. Sepulveda, B. J. Roth, and J. Wikswo, Biophys. J. **55**, 987 (1989).
[47]S. Rossi and B. E. Griffith, Chaos **27**, 093926 (2017).
[48]D. R. Hochbaum, Y. Zhao, S. L. Farhi, N. Klapoetke, C. A. Werley, V. Kapoor, P. Zou, J. M. Kralj, D. Maclaurin *et al.*, Nat. Methods **11**, 825 (2014).
[49]P. Sundaram, A. Nummenmaa, W. Wells, D. Orbach, D. Orringer, R. Mulkern, and Y. Okada, NeuroImage **132**, 477 (2016).
[50]S. J. Ihle, S. Girardin, T. Felder, T. Ruff, J. Hengsteler, J. Duru, S. Weaver, C. Forró, and J. Vörös, Biosens. Bioelectron. **201**, 113896 (2022).
[51]A. M. Edmonds, C. A. Hart, M. J. Turner, P.-O. Colard, J. M. Schloss, K. S. Olsson, R. Trubko, M. L. Markham, A. Rathmill *et al.*, Mater. Quantum Technol. **1**, 025001 (2021).
[52]T.-L. Wee, Y.-K. Tzeng, C.-C. Han, H.-C. Chang, W. Fann, J.-H. Hsu, K.-M. Chen, and Y.-C. Yu, J. Phys. Chem. A **111**, 9379 (2007).
[53]P. Balasubramanian, C. Osterkamp, Y. Chen, X. Chen, T. Teraji, E. Wu, B. Naydenov, and F. Jelezko, Nano Lett. **19**, 6681 (2019).
[54]S. J. DeVience, L. M. Pham, I. Lovchinsky, A. O. Sushkov, N. Bar-Gill, C. Belthangady, F. Casola, M. Corbett, H. Zhang *et al.*, Nat. Nanotechnol. **10**, 129 (2015).
[55]N. Arunkumar, K. S. Olsson, J. T. Oon, C. A. Hart, D. B. Bucher, D. R. Glenn, M. D. Lukin, H. Park, D. Ham *et al.*, Phys. Rev. Lett. **131**, 100801 (2023).